DIRECT NUMERICAL SIMULATION OF HYPERPYCNAL FLOWS IN OPEN-CHANNEL CONFIGURATION

3 authors:

Ricardo Andre Schuh Frantz
Ecole Nationale Supérieure d'Arts et Métiers
2 PUBLICATIONS   **0** CITATIONS

SEE PROFILE

Sylvain Laizet
Imperial College London
75 PUBLICATIONS   **957** CITATIONS

SEE PROFILE

Jorge Silvestrini
Pontifícia Universidade Católica do Rio Grande do Sul
59 PUBLICATIONS   **361** CITATIONS

SEE PROFILE

Some of the authors of this publication are also working on these related projects:

Bayesian Optimisation of Wall Blowing for Drag Reduction of a Turbulent Boundary Layer View project

An extended framework for turbulence-resolving simulations of (stratified) flows under the Boussinesq approximation View project

DIRECT NUMERICAL SIMULATION OF HYPERPYCNAL FLOWS IN OPEN-CHANNEL CONFIGURATION

Ricardo André Schuh Frantz, ricardo.frantz@acad.pucrs.br

Faculdade de Engenharia, Pontifícia Universidade Católica do Rio Grande do Sul, Av. Ipiranga 6681, 90619-900 Porto Alegre/RS, Brasil

Sylvain Laizet, s.laizet@imperial.ac.uk

Turbulence, Mixing and Flow Control Group, Department of Aeronautics, Imperial College London, London SW7 2AZ, United Kingdom

Jorge Hugo Silvestrini, jorgehs@pucrs.br

Faculdade de Engenharia, Pontifícia Universidade Católica do Rio Grande do Sul, Av. Ipiranga 6681, 90619-900 Porto Alegre/RS, Brasil

Abstract. *This numerical study introduces an open-channel configuration for direct numerical simulation of gravitational flows. The methodology proposes a parametrized method for the initiation of gravity currents. Particle-laden Flows are generated controlling the influx of sediment-water mixture into a computational domain. We reproduce a surge-like and a quasi-steady case. Results show the formation of refined turbulent structures and a destabilisation, at the head of the current, with the growth of lobe-and-cleft structures. General flow features such as sedimentation rate, suspended mass and deposit profiles are obtained. The wall friction velocity and flow deposit footprint are also computed. The quasi-steady current simulation shows a reasonable agreement with experimental results.*

Keywords: *gravity currents, hyperpycnal, quasi-steady*

1. INTRODUCTION

Gravity currents are natural phenomena triggered by fluids of different densities coming into contact with one another in a gravitational field. They occur naturally in both subaerial (e.g. air masses, pyroclastic flows, and avalanches), and subaqueous environments (e.g. turbidity currents, ocean flows and debris flows) (Simpson, 1999). Turbidity currents and submarine sediment flows redistribute more sediment across the surface of the Earth than any other sediment flow process (Talling et al., 2015). Amy et al. (2007) report turbidites (deposits from turbidity currents) mapped at more than 1,600 km off Morocco's shore. As mentioned by Puig et al. (2014), even the passing of fisheries trawler ships can trigger turbidity currents.

Gravity currents are active topics of study in academia and industry. Many deep-water hydrocarbon reservoirs consist of its deposits. They can damage submarine structures (i.e., wellheads and pipelines) (Meiburg and Kneller, 2010). Recently, a catastrophic failure of a dam released up to 60 million cubic meters of iron waste, forming a highly-destructive hyperpycnal flow that devastated a city's district in Minas Gerais, Brazil travelling over 600 km on its way to the ocean (G1, 2015; Terra, 2016).

Direct numerical simulations are employed here to investigate turbulent flows in the hyperpycnal regime. Bates (1953) introduced this concept in oceanographic aspects of delta formation to explain the inflow of a turbidity current into a basin (like rivers in a flood), where the inflow has a higher density than the fluid surrounding it and the current propagates close to the ocean floor (forming a underflow). For a deeper understanding of this phenomenon, laboratory experiments and computer simulations are heavily carried worldwide. Experimental data is fundamental for the validation of numerical simulations, assuring that models and simplifications retain the main physical features. According to Mulder and Alexander (2001), subaqueous sediment transport flows can be subdivided by their durations into surges, surge-like flows and quasi-steady currents (sometimes called initiation mechanism).

Espath et al. (2014, 2015) investigate the Reynolds number and fall velocity influence on surge-like flows, validating their results with experimental data and showing budgets depicting potential energy conversion to turbulent and particle-related dissipations on the configuration known as lock-exchange. On this closed configuration, a fixed-volume of a fluid mixture is enclosed by a gate in a lateral region of a domain. At $t > 0$, the gate is removed, and the current propagates due to the presence of gravity. Nasr-Azadani et al. (2013) investigated obstacle interactions in very similar configurations showing little effects on the front location evolution and strong effects on deposit. Lock-exchange simulations of particle-laden flows cannot reach steady-state regime. Therefore time averaging is not possible, as a flow is denoted quasi-steady if there are no significant changes in the velocity field through time.

Fick et al. (2015) performed a series of highly equipped laboratory experiments to identify transport and deposition mechanisms for flows with different particle volume concentrations. They produced currents by releasing a water-sediment mixture with a controlled flow-rate. Their results were image-recorded and velocity and concentration profiles measured at both upstream and downstream locations.

The present configuration evolved from the typical lock-exchange configuration (Härtel et al., 2000b; Necker et al.,
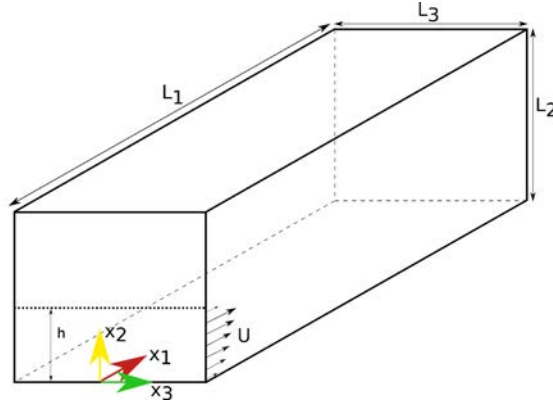
Figure 1: Schematic view of the proposed computational domain.

2002) and investigates an open-channel with controlled fluid injection. This computational methodology not only allows to recreate lock-exchange surge-like flows but also to compute steady-state flows. Turbidity currents have not yet been fully investigated with DNS in this regime but, as stated before, are common in experimental research.

According to Hogg et al. (2016) flows from sustained sources have been less investigated, despite allowing the identification of time and length scales at which mixing transitions occur and the speed of the front flow. This work compares simulations in similar regime aiming to present a unified methodology with better fluid influx control, as well as comparing a quasi-steady simulation with a surge-like flow.

2. FLOW CONFIGURATION AND GOVERNING EQUATIONS

We employ the incompressible Navier-Stokes equations to model low-concentration flows (i.e. turbidity currents) with volume fractions of $O(1\%)$. This allows the use of Boussinesq approximation, a simplification that considers density variations only in the buoyancy terms, reducing the computational cost of the simulation. To model particle transport, an extra convection-diffusion equation, on a Eulerian-fashion (neglecting particle-particle interactions), couples the concentration field with the momentum equation. Dimensionless equations are given by

$$\frac{\partial u_j}{\partial x_j} = 0, \tag{1}$$

$$\frac{\partial u_i}{\partial t} = - u_j \frac{\partial u_i}{\partial x_j} - \frac{\partial p}{\partial x_i} + \frac{1}{Re} \frac{\partial^2 u_i}{\partial x_j \partial x_j} + e_i^g Ri\, c, \tag{2}$$

$$\frac{\partial c}{\partial t} = - (u_j + u_s e_j^g) \frac{\partial c}{\partial x_j} + \frac{1}{Re\, Sc} \frac{\partial^2 c}{\partial x_j \partial x_j}. \tag{3}$$

Quantities u_i, p and c represent the three-dimensional flow velocity, pressure, and particle concentration fields respectively. For each simulation, a fixed Reynolds number is defined as $Re = Uh/\nu$, where U is the inlet maximum velocity, h represents an averaged current height (the window height, see Fig. (1)) and ν the fluid kinematic viscosity (in our case, that of the water). The Schmidt number is defined as $Sc = \nu/D$, where D is the particle's mass diffusivity, and kept as one not to increase computational cost.

A constant overall Richardson number is given by $Ri = g'\, h/U^2$ where the reduced gravity is given by the density excess $g' = [g\, (\rho_p - \rho_f)/\rho_f]\varphi$ with g as the module of the gravitational acceleration and φ the diluted particle volume fraction. The Richardson number can also be expressed as the Froude number, $Fr = 1/\sqrt{Ri}$, and is a important parameter strongly affecting the current dynamics. The vector $e_i^g = (0, -1, 0)$ is a unitary vector with the same direction as the gravitational acceleration g. Constant u_s is a normalised particle settling velocity obtained by the Stokes settling velocity law (Julien, 2010) for a given particle diameter. Bed deformations due to deposit, erosion, and resuspension of material are neglected.

The parameter H represents half of waterline height and is used to define the channel non-dimensional size as $L_1 \times L_2 \times L_3 = 16 \times 2 \times 2$. An aspect-ratio relation H/h of 1.6 was respected in order to match the experimental set-up. The initial condition, there is a domain filled with clean fluid (of density ρ_f) at rest. The computational domain is discretised on a Cartesian mesh of $n_1 \times n_2 \times n_3$ nodes. Figure 1 is a scheme of the proposed configuration. An open configuration requires inflow/outflow boundary conditions in the stream-wise direction of the flow. A water/particles mixture is influxed
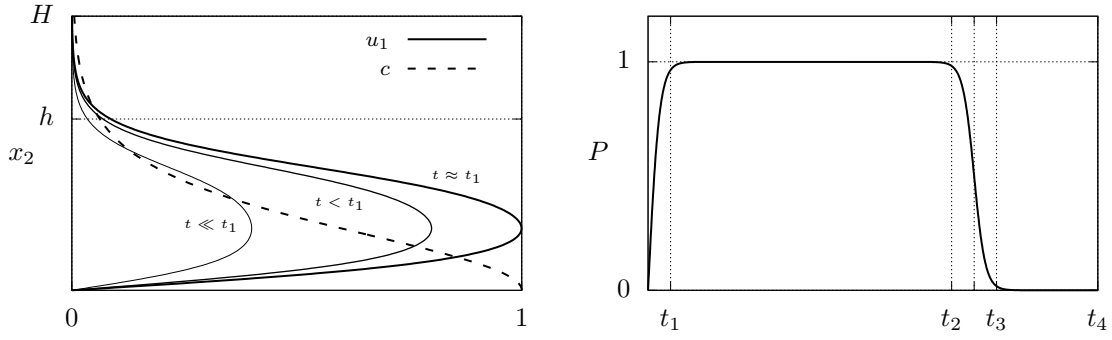
Figure 2: Concentration profiles and velocity as function of time and the vertical direction (left). Influx control function as function of time (right).

into the domain, after the first time step, via a Dirichlet boundary condition describing a particle concentration and a velocity profile for the u_1 component on the $x_1 = 0$ plane. Inflow equations are

$$u_1(t, x_2) = \left\{ \frac{1}{\gamma_6} \tanh(\gamma_1 \, x_2)[\gamma_2 + \gamma_3 \tanh(\gamma_4 \, x_2 + \gamma_5)] \right\} P(t), \tag{4}$$

$$c(t, x_2) = \text{sech}^2(\gamma_7 \, x_2) \quad \text{if} \quad t \leq t_3. \tag{5}$$

The release of mixture is controlled by an influx function given by

$$P(t) = \tanh\left(\frac{2t}{t_1} \right) \left(0.5 - 0.5 \tanh\left(\frac{-2t + t_2 + t_3}{t_2 - t_3} \right) \right) \tag{6}$$

where the value t_1 is the time for the maximum flow rate, t_2 is the time when the flow rate starts to decrease, t_3 when it stops and t_4 denotes the final simulation time. Equations (4), (5) and (6) are obtained by fitting and normalising experimental data profiles and the flow rate measurements from Fick et al. (2015). The constants γ_ℓ ($\ell = 1...7$) give the profile forms shown in Fig. (2). Here a non-dimensional instantaneous flow rate can be approximated as $Q(t) = hL_3\overline{u_1} \, P(t)$ with $\overline{u_1}$ representing a bulk velocity. An outflow condition, modelled as a one-dimensional convection equation, is imposed at the end of the channel. It has the form

$$\frac{\partial \Phi}{\partial t} + U_b \frac{\partial \Phi}{\partial x_1} = 0 \tag{7}$$

where Φ represents velocity components u_i and particles fraction c. In all cases, the convective velocity U_b is fixed as one. Channel laterals are set to periodic boundary conditions. Both top and bottom are set to walls (no-slip) for velocity. For the concentration a no-flux condition is imposed at the top, while in bottom a deposit condition is emulated by the following equation

$$\frac{\partial c}{\partial t} + u_s e_2^g \frac{\partial c}{\partial x_2} = 0. \tag{8}$$

A random noise $O(5\%)$ is superimposed to all velocity components at the inlet region (for $t > 0$) to trigger three-dimensional effects.

3. NUMERICAL METHODS AND PARAMETERS

The 3D DNS results presented in this work are carried out with `Incompact3d`[1], a solver dedicated to DNS/LES of turbulent flows. The same is based on high-order compact schemes (Lele, 1992), with quasi-spectral accuracy, for first and second spatial derivatives. The given behaviour is due to its capabilities of representing a wide range of scales accurately. The convective terms are written in the skew-symmetric form for reducing aliasing errors. A third-order Adams-Bashforth scheme is used for time integration (Laizet and Lamballais, 2009, 2011). The code was built on top of `2DECOMP&FFT`[2] a scalable two-dimensional domain decomposition library used to improve computational efficiency

---

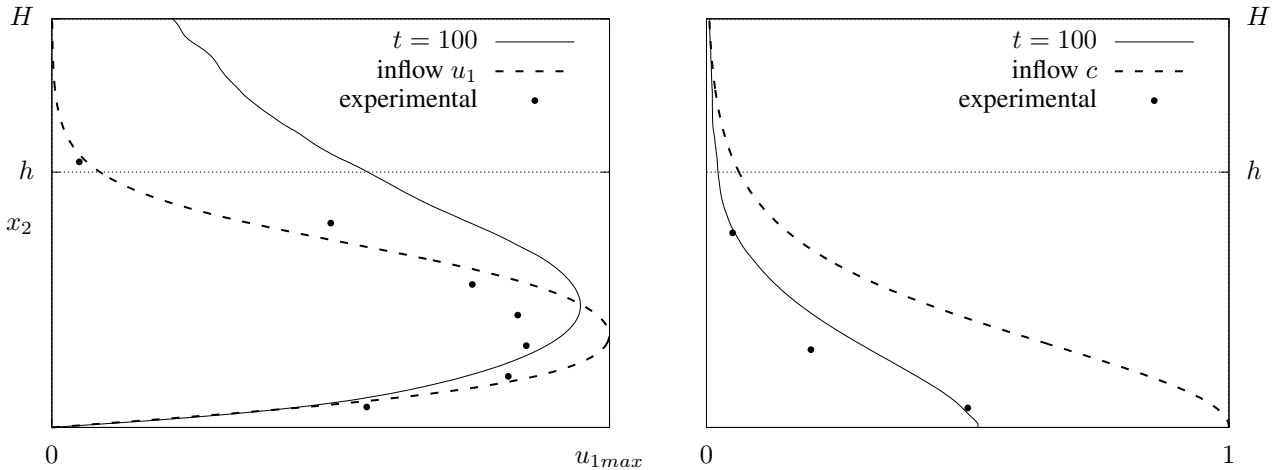[1]Available at `www.incompact3d.com`.
[2]Available at `www.2decomp.org`.

Figure 3: Comparison between the final time of simulation case QS against averaged experimental results. Longitudinal velocity (left) and concentration (right).

in scalability in shared-memory clusters. It has been successfully tested with up to thousands of cores (Li and Laizet, 2010). The Intel Math Kernel Library (MKL) was used to improve the performance of Intel architecture systems on the 3D Fast Fourier Transforms (FFTs) required to solve the Poisson equation completely in the spectral space. Simulations were performed on LAD facility at PUCRS with 192 physical Xeon cores requiring a week of wall-clock time and over a terabyte of storage. Two cases, both with $Re = 8000$, $Ri = 1.2$, $u_s = 0.015$ simulated in a domain with dimensions $L_1, L_2, L_3 = (16, 2, 2)$, discretised with $n_1, n_2, n_3 = (1921, 241, 240)$ nodes, and time-step of 10^{-3}. The inflow parameters for for the first case (QS) are $t_1, t_2, t_3, t_4 = (0.5, 99.5, 100, 100)$ and for the second case (S) are $t_1, t_2, t_3, t_4 = (0.5, 9.5, 10, 70)$. Here S stands for a surge flow, generated by a short inflow interval, while QS stands for a case with a sustained influx reaching a quasi-steady state.

4. RESULTS

Results for both cases are presented in this section. Figure 3 compares results of the QS case at final simulation time, $t_{4QS} = 100$, for both steam-wise velocity and particle concentration, against the inflow conditions and averaged experimental results. Profiles are captured at a fixed upstream position equivalent in the computational and experimental channel. Velocity show a good agreement close to the wall, but differs for $x_2 \geqslant h$. Concentration values show reasonable agreement with experimental results. As we can see in Fig. (4), the early flow evolution is governed by the emergence of bi-dimensional Kelvin-Helmholtz vortices for both cases.

These billows are generated right on the shearing interface between the moving current and the resting ambient fluid, as the absorbed ambient fluid mixes with the current body. The passage of the head leaves a mixing layer of low concentration fluid on top of the current. For $t > 5$ we also observe the initial emergence of three-dimensional lobe-and-cleft structures on the head, this is mainly due to ambient fluid entanglement with the frontal interface. Lobe-and-cleft instabilities are responsible for the resulting coherent deposit structures (or channel-like) at the bottom and are of great interest as this formation are very similar to submarine canyons (Härtel et al., 2000a).

Mixing occurs also below the current. A mixing zone underneath the head occurs because the flow overruns into ambient fluid, generating a re-circulation zone that is trapped close to the ground, right behind the head. We observe that for longer inflow time (QS), the extra fluid mixture being in-fluxed replaces the head loss, transporting the frontal interface out of the channel. In the other hand, we observe a completely dissipation of the head on the case S.

Figure 5 illustrates vortical structures at the developing head of the current using Q-criterion (Dubief and Delcayre, 2000) for an iso-value of $Q = 2$ at $t = 15$. A positive Q-criterion value implies that the flow is dominated locally by fluid rotation allowing the visualisation of vortex tubes (Nasr-Azadani and Meiburg, 2014).

Results show strong homogeneity in the spatial direction x_3 as the domain is a horizontal channel with periodic laterals. Instantaneous averaged planes are shown in Fig. (6) for the velocity components and concentration.
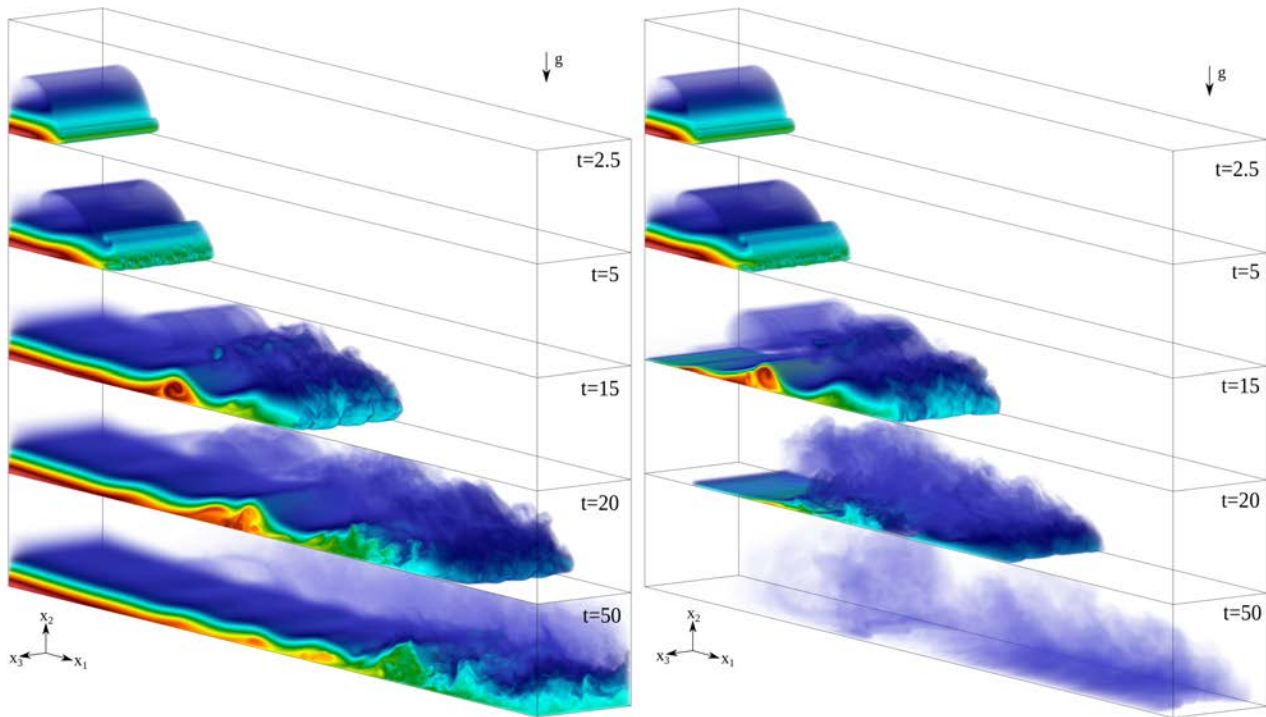
Figure 4: Spatiotemporal evolution of the current by volume renderings of the concentration field x. Case QS (left) and S (right) where red is one and blue values greater than zero.
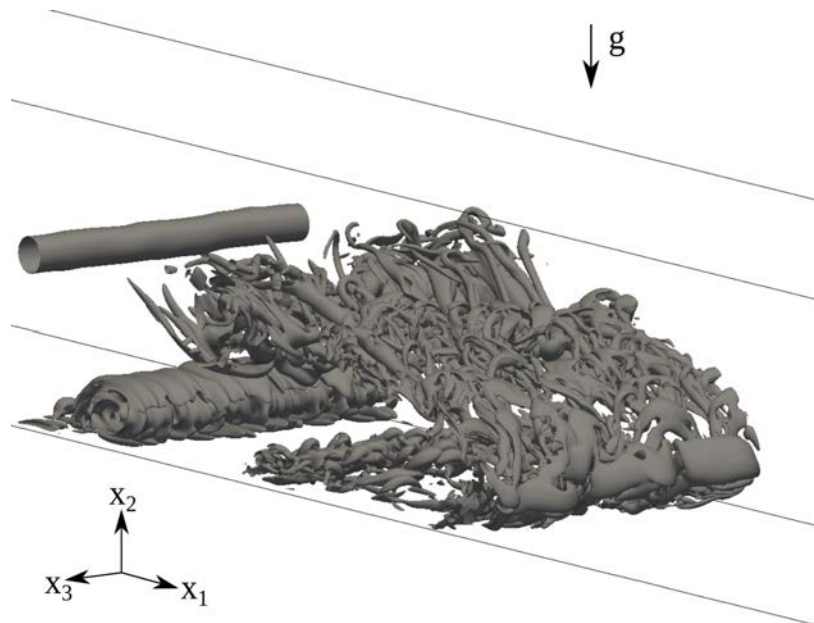

Figure 5: Turbulent structures visualisation by a Q-criterion iso-surface of case S.
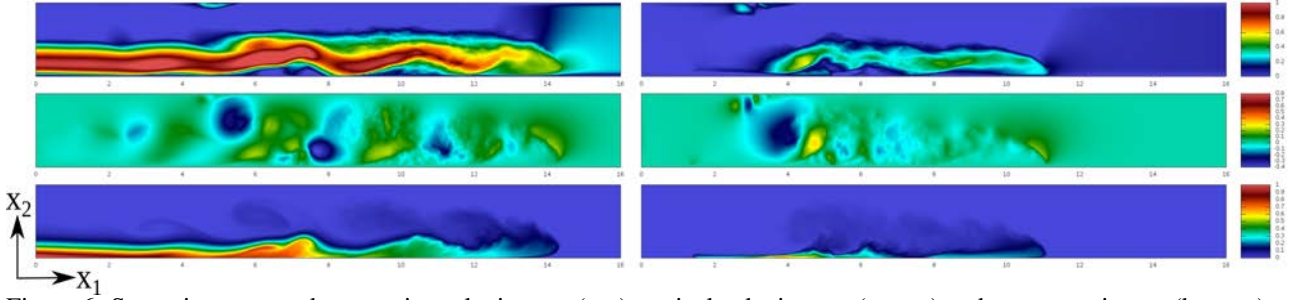
Figure 6: Spanwise-averaged steamwise velocity, u_1, (top) vertical velocity, u_2, (centre) and concentration, c, (bottom) at $t = 25$. Case QS (left) and S (right).

4.1 GENERAL FEATURES OF THE FLOW

In this section, general flow features are compared for the two cases. Figure 6 shows span-wise planes for the concentration field c and velocity components u_1 and u_2 for a given time $t = 25$. Averaging in the given direction is possible due to using periodic laterals and results in a more meaningful visualisation. To illustrate the effect of Eq. (8) that allows particles, reaching the bed of the channel, to leave the domain with settling speed u_s creating a virtual sedimentation effect on the simulation. This is shown on Fig. (7) with the sedimentation rate, $\dot{m}_s$, representing the temporal evolution of the particle-loss trough the channel's bed, and obtained by

$$\dot{m}_s(t) = \frac{1}{L_1 L_3} \int_0^{L_1} \int_0^{L_3} c(x_1, x_2 = 0, x_3, t) u_s dx_3 dx_1. \tag{9}$$

On the other hand, Fig. (7) (right) shows the evolution of total mass of particles influxed into the domain that are still in suspension. This is computed by a volume integral of the particles field c, given by

$$m_s(t) = \int_V c(x_1, x_2, x_3, t) dV. \tag{10}$$

The marker t_{3S} points out the end of injection on the S case. The temporal evolution of the head of the current (or the front location) x_{1f} correspond to the further stream-wise position where the concentration is greater than 1%. This is
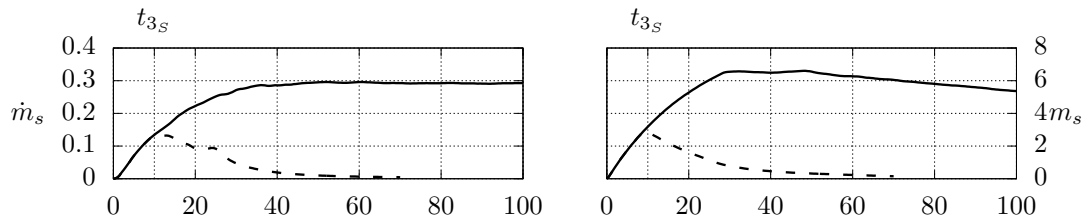

Figure 7: Sedimentation rate $\dot{m}_s(t)$ (left) and suspended particle mass $m_s(t)$ (right) both as function of time. Continuous (–) line corresponds to QS while dashed (- -) to S case.
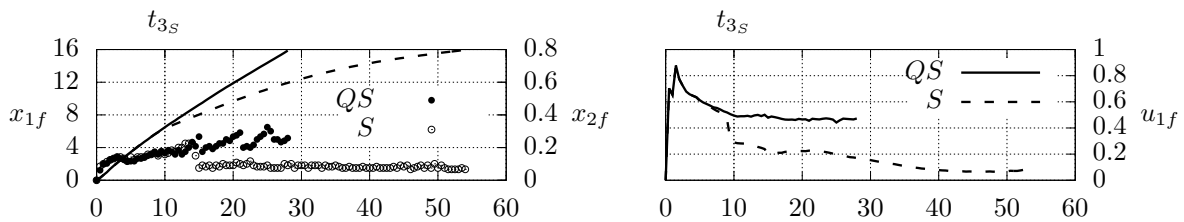

Figure 8: Evolution of the front location coordinates x_{1f}, x_{2f} (left) and the corresponding averaged front velocity $u_1(x_{1f}, x_{2f})$ (right). Continuous (–) line corresponds to QS while dashed (- -) to S case.
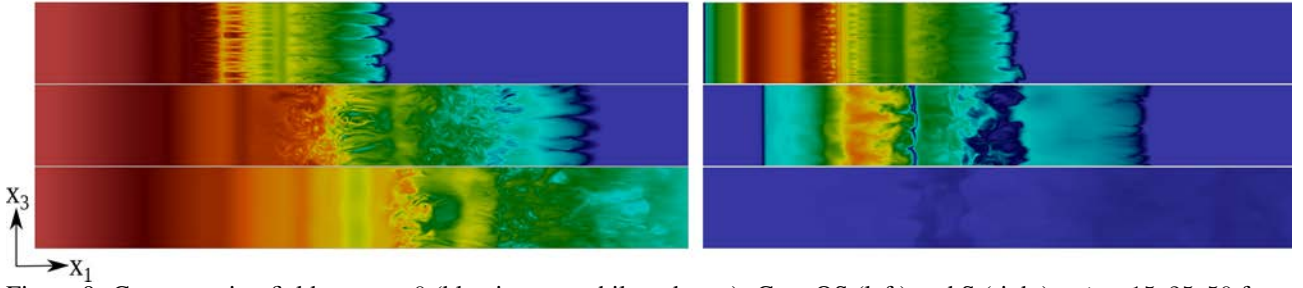
Figure 9: Concentration field at $x_2 = 0$ (blue is zero, while red, one). Case QS (left) and S (right) at $t = 15, 25, 50$ from top to bottom.
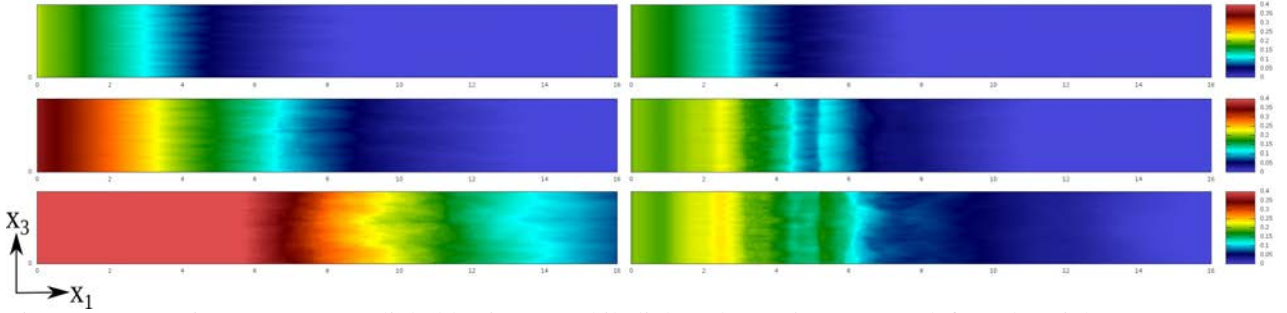

Figure 10: Deposit map at $x_2 = 0$ (light blue is zero, while light red, 0.015). Case QS (left) and S (right) at $t = 15, 25, 50$ from top to bottom.

obtained by counter stream-wise scanning (from outlet to inlet) an averaged two-dimensional plane (see Fig. (6)) of the concentration field c for each time. Figure 8 shows the temporal evolution of the front coordinates x_{1f}, x_{2f} (left) and also the corresponding averaged current speed $u_1 f$ (right). We observe that the the QS case shows a front velocity converge to a value of 0.43 while the S case show a significant deceleration after t_{3S}.

4.2 BOTTOM WALL EFFECTS

This section highlights how the current affects the bottom plane of the channel. Figure 9 exposes the concentration field c at $x_2 = 0$ for both cases at different times. We can observe that deposit is not occurring at the turbulent head section.

Figure 10 depicts a deposit map on the $x_2 = 0$ plane and represent the quantity of material that left the domain along plane (x_1, x_3) are obtained by

$$D(x_1, x_3, t) = \int_0^t c(x_1, x_2 = 0, x_3, \tau) u_s d\tau. \tag{11}$$

Figure 11 illustrates the formation, merging and splitting of the lobe-and-cleft instabilities in the bottom, this can be seen as the footprint of the turbidity current. There is 0.8 time between each isoline, we can see that the distance between them remains constant for the QS case (top) and decreases in the S case after time $t = 10$ when the injection stops and the flow start to decelerate.

Figure 12 reveals dimensionless friction (or shear) velocity at the bottom, simply obtained by extracting square root of the velocity gradient at the wall as

$$u_\tau = \sqrt{\tau_w} \text{ with } \tau_w = \frac{1}{Re} \sqrt{\left(\frac{\partial u_1}{\partial x_2}\right)^2 + \left(\frac{\partial u_3}{\partial x_2}\right)^2}\Big|_{x_2=0}. \tag{12}$$

According to Necker et al. (2002) this can estimates the flow erosive potential, where values greater than a critical threshold could be regions of bed remobilization. This initial results show that sustained currents, such as the QS case, may have a higher erosive potential than surge-like flows.

5. CONCLUSIONS

This work proposed an open channel configuration for simulating particle-laden flows over a flat bed and compares two three-dimensional DNS cases of hyperpycnal turbidity currents. The methodology can produce from surges to quasi-steady state flows in a unified computational configuration by controlling the influx of water mixture with a pulse like
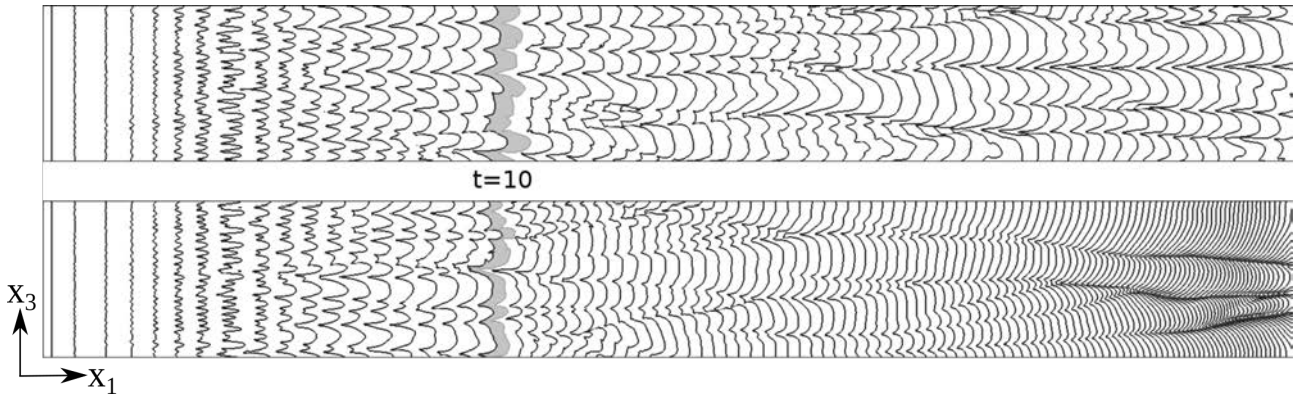
Figure 11: Formation, merging and splitting of lobe-and-cleft structures shown on concentration contours of $c = 0.01$ at the bottom plane of the domain with x_1. This image is also known as the current footprint. Case QS (top) and S (bottom).
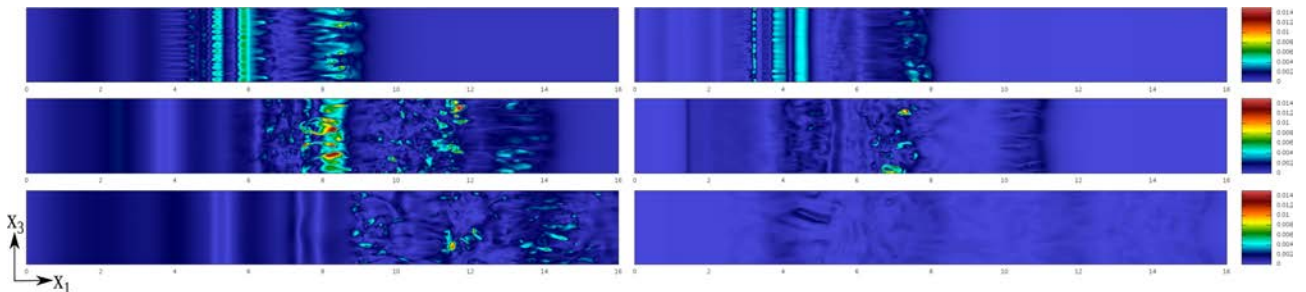

Figure 12: Shear friction map at $x_2 = 0$ (light blue is zero and light red is 0.015). Case QS (left) and S (right) at $t = 15, 25, 50$ from top to bottom.

function. This opens up other possibilities for validation as it comes closer to experimental set-ups, a required step for incorporating more complex and realistic physics. In the results, the first simulation (case QS) reaches steady-state for $t > 30$, while the second (case S) emulates a lock-exchange like a case, injecting a finite volume of fluid mixture into the domain and fully depositing particles. By comparing deposit maps, Fig. (10), with the concentration field, Fig. (9), for a given position, we observe that deposit are unlikely to occur in the highly turbulent head section. This behaviour can be directly associated with higher values of shear friction velocity, acting as a lifting force (on the x_2 direction) and suppressing the deposition. From analysing the footprint of the current, Fig. (11), seems necessary to improve the inflow perturbation as in the early regime the white noise is overcoming the unstable modes growing on the current. Besides, the introduction of a customised derivative scheme for handling the top wall as a fixed boundary will reduce confinement effects imposed by the no-slip surface, and may improve the agreement with experimental results.

6. ACKNOWLEDGEMENTS

7. REFERENCES

Amy, L. A., Benetti, S., Weaver, P. P. E., Georgiopoulou, A., and Zu, C. (2007). Onset of submarine debris flow deposition far from original giant landslide. *Nature*, 450(November):541–544.

Bates, C. (1953). A Rational Theory of Delta Formation. *Journal of Sedimentary Research*, 37(9):132–139.

Dubief, Y. and Delcayre, F. (2000). On coherent-vortex identification in turbulence. *Journal of Turbulence*, 1(January):1–22.

Espath, L. F. R., Pinto, L. C., Laizet, S., and Silvestrini, J. H. (2014). Two- and three-dimensional Direct Numerical Simulation of particle-laden gravity currents. *Computers and Geosciences*, 63:9–16.

Espath, L. F. R., Pinto, L. C., Laizet, S., and Silvestrini, J. H. (2015). High-fidelity simulations of the lobe-and-cleft structures and the deposition map in particle-driven gravity currents. *Physics of Fluids*, 27(5):056604.

Fick, C., Boffo, C. H., Moraes, M. A. S., Manica, R., and Borges, A. L. D. O. (2015). Mechanisms of transport and deposition of high-concentrated density currents: A detailed approach to hydrodynamic and depositional features. In

Abstracts of 31st IAS Meeting of Sedimentology held in Krakow on 22nd 25th of June 2015. Polish Geological Society, page 176, Kraków, Poland.

G1 (2015). Barragem se rompe, e enxurrada de lama destrói distrito de Mariana.

Härtel, C., Carlsson, F., and Thunblom, M. (2000a). Analysis and direct numerical simulation of the flow at a gravity-current head. Part 2. The lobe-and-cleft instability. *Journal of Fluid Mechanics*, 418:213–229.

Härtel, C., Meiburg, E., and Necker, F. (2000b). Analysis and direct numerical simulation of the flow at a gravity-current head. Part 1. Flow topology and front speed for slip and no-slip boundaries.

Hogg, A. J., Nasr-Azadani, M. M., Ungarish, M., and Meiburg, E. (2016). Sustained gravity currents in a channel. *Journal of Fluid Mechanics*, 798:853–888.

Julien, P. Y. (2010). *Erosion and sedimentation*. Cambridge University Press.

Kneller, B. and Buckee, C. (2000). The structure and fluid mechanics of turbidity currents: a review of some recent studies and their geological implications. *Sedimentology*, 47:62–94.

Laizet, S. and Lamballais, E. (2009). High-order compact schemes for incompressible flows: A simple and efficient method with quasi-spectral accuracy. *Journal of Computational Physics*, 228.

Laizet, S. and Lamballais, E. (2011). Incompact3D User Guide. Technical report, Imperial College London, London.

Lele, S. K. (1992). Compact finite difference schemes with spectral-like resolution. *Journal of Computational Physics*, 103(1):16–42.

Li, N. and Laizet, S. (2010). 2DECOMP & FFT-A Highly Scalable 2D Decomposition Library and FFT Interface. *Cray User Group 2010 conference*, pages 1–13.

Meiburg, E. and Kneller, B. (2010). Turbidity Currents and Their Deposits. *Annual Review of Fluid Mechanics*, 42:135–156.

Mulder, T. and Alexander, J. (2001). The physical character of subaqueous sedimentary density flow and their deposits. *Sedimentology*, 48(2):269–299.

Nasr-Azadani, M. M., Hall, B., and Meiburg, E. (2013). Polydisperse turbidity currents propagating over complex topography: Comparison of experimental and depth-resolved simulation results. *Computers and Geosciences*, 53:141–153.

Nasr-Azadani, M. M. and Meiburg, E. (2014). Turbidity currents interacting with three-dimensional seafloor topography. *Journal of Fluid Mechanics*, 745:409–443.

Necker, F., Härtel, C., Kleiser, L., and Meiburg, E. (2002). High-resolution simulations of particle-driven gravity currents. *International Journal of Multiphase Flow*, 28(2):279–300.

Puig, P., Palanques, A., and Mart, J. (2014). Contemporary Sediment-Transport Processes in Submarine Canyons. *Annual Review of Marine Science*, pages 53–77.

Simpson, J. E. (1999). *Gravity currents: In the Environment and the Laboratory*. Cambridge University Press, 2 edition.

Talling, P. J., Allin, J., Armitage, D. A., Arnott, R. W., Cartigny, M. J., Clare, M. A., Felletti, F., Covault, J. A., Girardclos, S., Hansen, E., Hill, P. R., Hiscott, R. N., Hogg, A. J., Hughes Clarke, J., Jobe, Z. R., Malgesini, G., and Mozzato, A. (2015). Key Future Directions for Research on Turbidity Currents and Their Deposits. *Journal of Sedimentary Research*, 85(February):153–169.

Terra (2016). Desastre em Mariana é o maior acidente mundial com barragens.